nature electronics

Supplementary information

https://doi.org/10.1038/s41928-026-01708-y

In situ monitoring of channel swelling in organic electrochemical transistors using a laser Doppler vibrometer

In the format provided by the authors and unedited

Table of contents

Supplementary Tables 1-5

Supplementary Note 1. The principle of the LDV-M. The system is based on a heterodyne interferometer architecture employing an Acousto-Optic Modulator (AOM) to generate a high-frequency carrier. This configuration allows for the simultaneous extraction of two physical quantities from the backscattered signal: velocity is derived from the frequency deviation (Doppler shift, $f_D = 2v/\lambda$) of the carrier, while displacement (height) is determined from the phase shift ($\Delta\phi$) of the heterodyne carrier via digital fringe counting or phase demodulation, which directly corresponds to the optical path length change ($d = \Delta\phi \cdot \lambda/4$)[1,2].

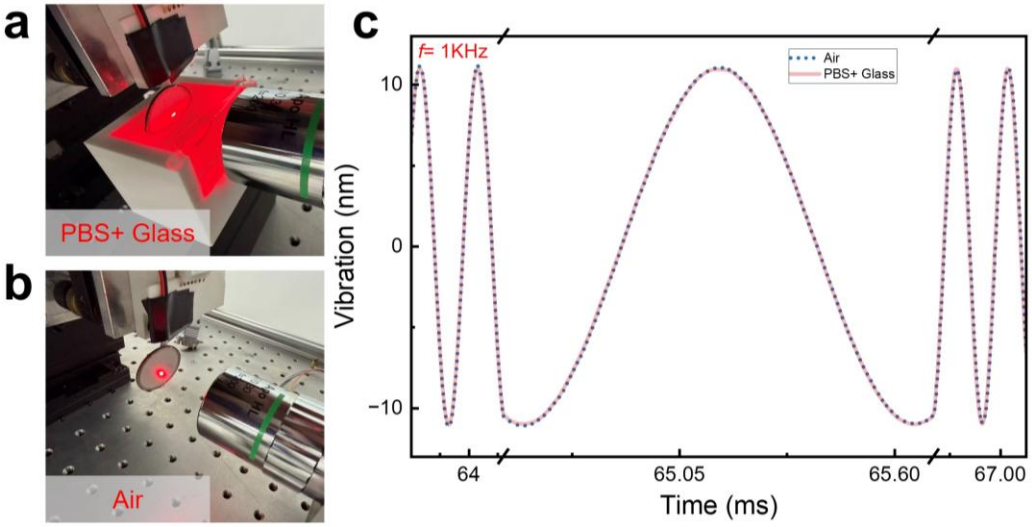

Supplementary Fig. 1. Influence of Electrolyte Solution on Swelling Measurements. Laser focused on the PZT surface **(a)** through a glass and 1× PBS solution or **(b)** only through air. **c,** Comparison of measured vibration amplitudes of the PZT through LDV-M driven at 1 kHz switching frequency under these two conditions.

We measured the vibration amplitude of the actuator at a fixed drive voltage under two conditions: (i) actuator exposed directly to air, and (ii) actuator immersed in 1× PBS solution along with a 0.7 mm glass slide in the laser pathway (mimicking our OECT channel swelling test setup). The deviation in vibration amplitude between these two conditions is essentially identical, with

vibration magnitudes measured with the two setups being 22.10±0.14 nm (bare actuator) and 22.01±0.06 nm (actuator in 1× PBS). This confirms that the introduction of liquid and glass into the laser pathway will not distort the measurement, ensuring its fidelity.

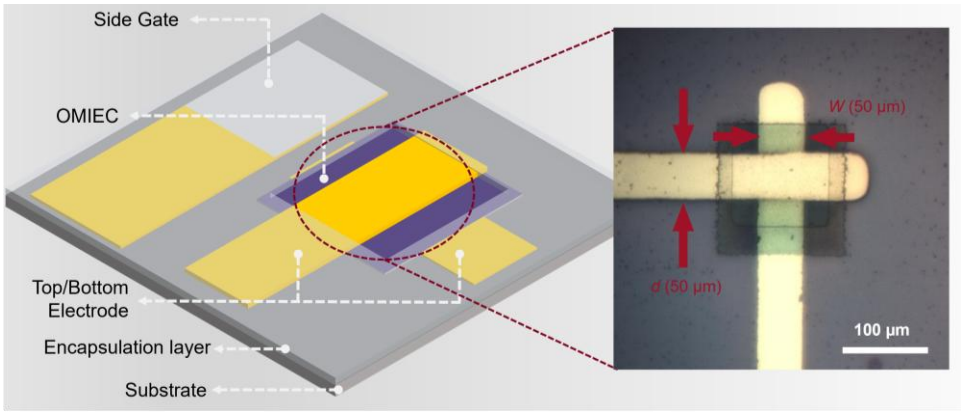

Supplementary Fig. 2. Side-gated vOECT architecture along with a microscope photo of the channel area.

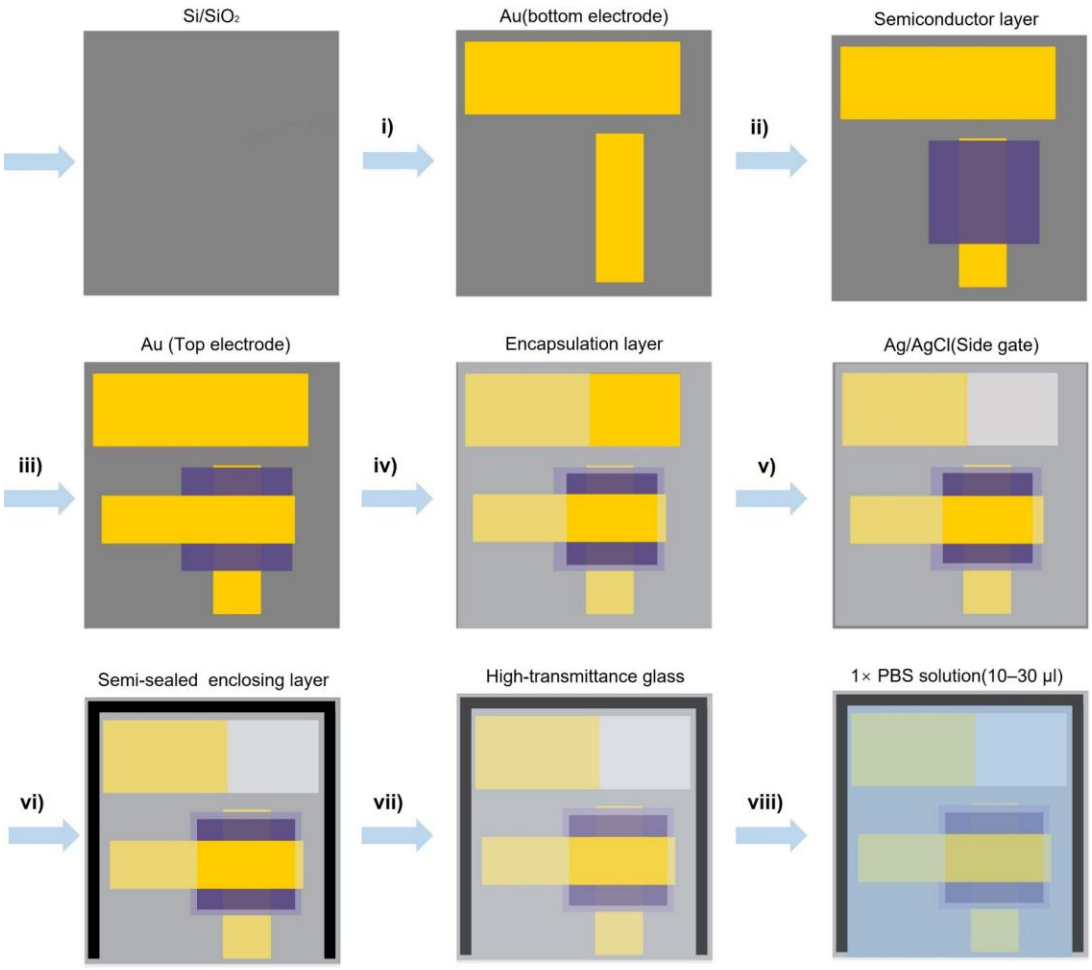

Supplementary Fig. 3. Fabrication process of the side-gated vOECT. i) Thermal evaporation of the bottom and gate electrodes with a shadow mask; ii) Spin-coating and photo-patterning of the p- or n-type OMIEC channel layer; iii) Thermal evaporation of the top electrode with a shadow mask; iv) Spin-coating and photopatterning of the SU-8 encapsulation layer, where the channel areas are left open. v) Drop casting of Ag/AgCl paste as the gate electrode; vi) Coating uncured PDMS solution around the device and adhering polyimide template (PI, with a thickness of 0.3 mm) to the PDMS; vii) Placing a high-transmittance glass (with a thickness of 0.7 mm) on the PI template to achieve semi-sealing of the device; viii) Application of 1× PBS solution (10–30 μL) into the vacancy between the glass and the vOECT.

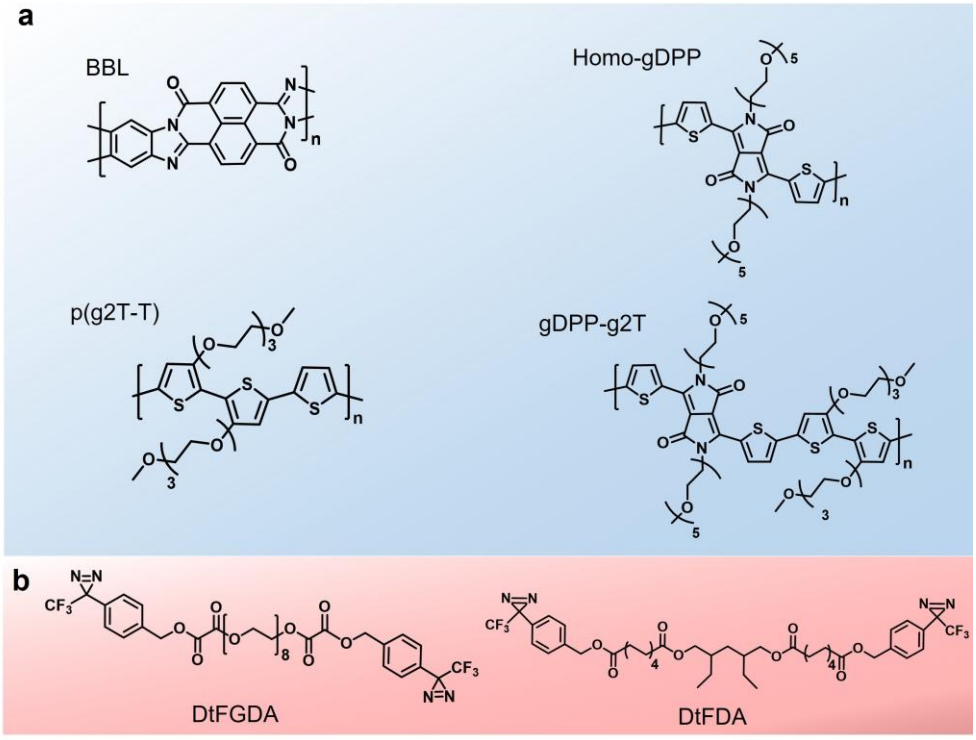

Supplementary Fig. 4. Chemical structures of the used materials. a, OMIECs, including BBL, Homo-gDPP, p(g2T-T), and gDPP-g2T. **b,** Crosslinkers, including GDA and DA.

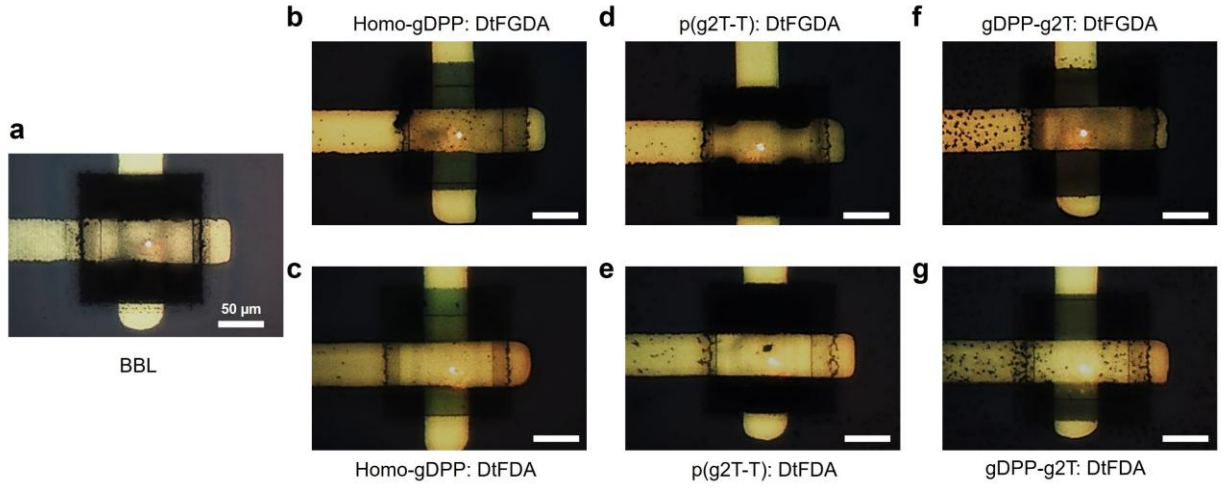

Supplementary Fig. 5. Laser spot position of LDV-M on vOECT channels with different OMIECs. (a)BBL; **(b)** Homo-gDPP:GDA; **(c)** Homo-gDPP:DA; **(d)** p(g2T-T):GDA; **(e)** p(g2T-T):DA; **(f)** gDPP-g2T:GDA; **(g)** gDPP-g2T:DA.

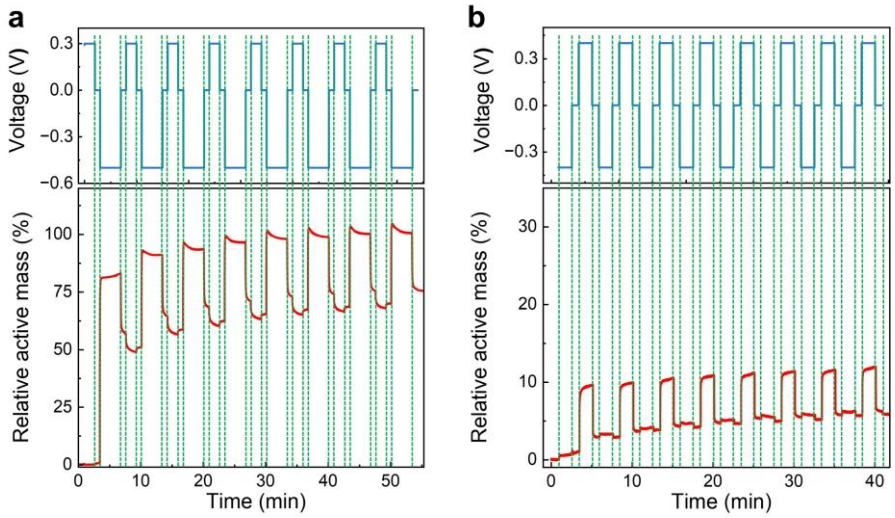

Supplementary Fig. 6. OMIEC film swelling characterized by EQCM. Relative active swelling responses of **(a)** BBL and **(b)** p(g2T-T):DA films under varying working electrode biases.

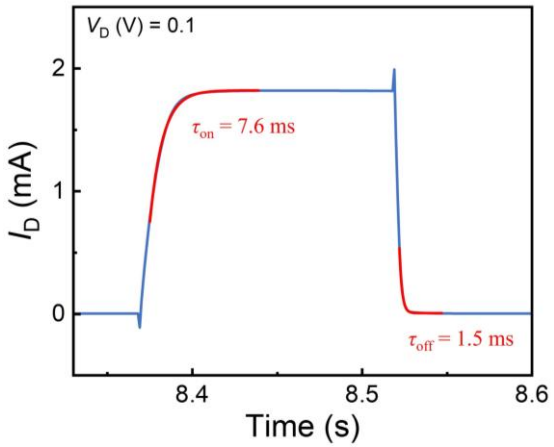

Supplementary Fig. 7. Schematic of switching transient time fitting for BBL-based vOECT. In this work, the switching time constants (τ_{on}, τ_{off}) for all materials were extracted by fitting the transient responses to an exponential function[3].

Supplementary Table 1. Summary of active swelling characteristics of different OMIECs.

Type	RC time	Original Film Thickness[a] (nm)	*f* = 3.3 Hz		*f* = 11.1 Hz		*f* = 111.1 Hz	
			Swelling Magnitude[b] (nm)	Swelling percentage[c]	Swelling Magnitude[b] (nm)	Swelling percentage[c]	Swelling Magnitude[b] (nm)	Swelling percentage[c]
BBL	7.6 ms (ON) 1.5 ms (OFF)	130.2±7.8	115.9±1.5	89.2±1.1%	106.6±1.8	82.0±1.4%	19.5±0.7	15.0±0.5%
Homo-gDPP: GDA	1.0ms (ON) 0.2 ms (OFF)	113.5±5.6	22.8±1.1	20.7±1.0%	22.2±1.7	20.2±1.5%	16.8±1.3	15.3±1.1%
Homo-gDPP: DA	5.8 ms (ON) 0.4 ms (OFF)	110.1±4.5	10.9±2.7	9.9±2.5%	9.0±1.6	8.2±1.5%	5.8±1.6	5.3±1.5%
p(g2T-T): GDA	0.8 ms (ON) 0.2 ms (OFF)	80.2±3.8	10.1±0.5	12.6±0.6%	8.8±0.6	11±0.8%	4.7±0.8	5.9±1.0%
p(g2T-T): DA	6.8 ms (ON) 0.8 ms (OFF)	78.8±3.1	4.1±0.2	5.1±0.3%	3.9±0.4	4.9±0.5%	2.5±0.4	3.1±0.5%
gDPP-g2T: GDA	2.6 ms (ON) 0.2 ms (OFF)	106.4±4.8	20.0±1.4	18.8±1.3%	17.5±1.8	16.5±1.7%	9.8±0.42	9.2±0.4%
gDPP-g2T: DA	6.7ms (ON) 0.5 ms (OFF)	104.1±5.1	7.6±1.3	7.1±1.2%	6.7±1.5	6.3±1.4%	4.9±1.0	4.6±0.9%

a) The original film thickness was characterized by AFM before the film made contact with the electrolyte.
b) Error bars represent standard deviation for n = 5, mean ± s.d.
c) Percentage of swelling magnitude compared to original film thickness.

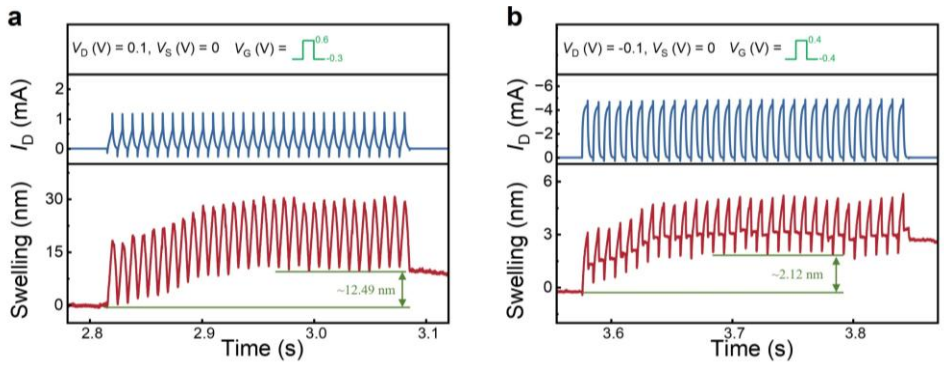

Supplementary Fig. 8. Swelling baseline shifts under 111.1 Hz switching frequencies. vOECTs based on **(a)** BBL and **(b)** p(g2T-T):DA, respectively.

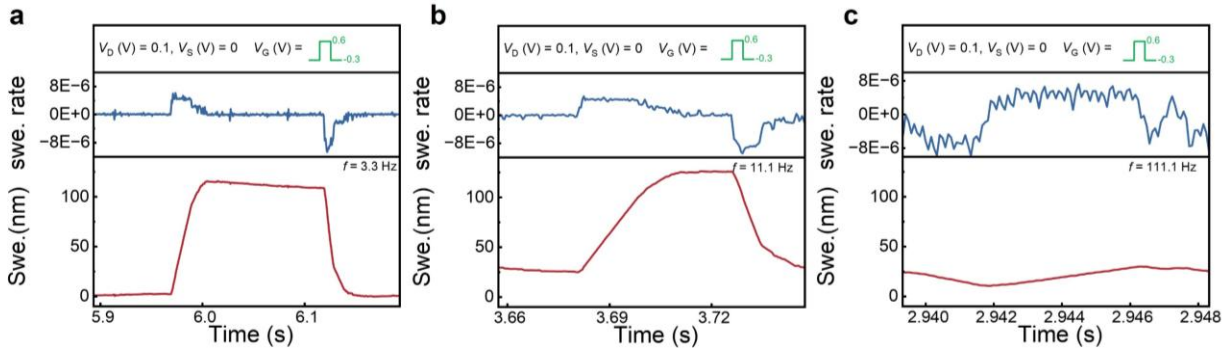

Supplementary Fig. 9. Active swelling rate of vOECT based on BBL. Active swelling rate at switching frequencies of **(a)** 3.3Hz, **(b)** 11.1Hz, and **(c)** 111.1Hz. The active swelling rate is calculated by taking the first-order derivative of the swelling curves under different operating frequencies.

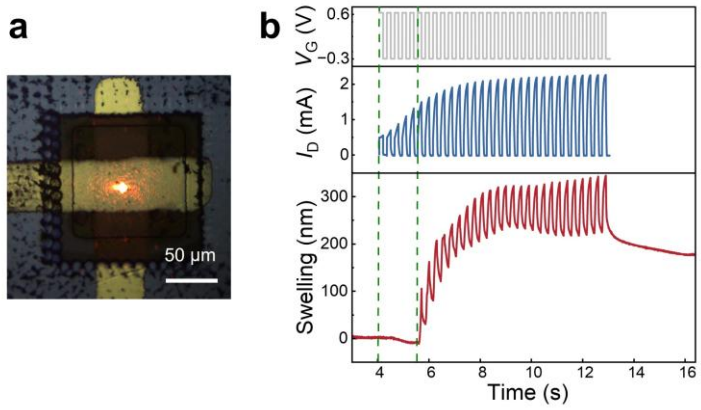

Supplementary Fig. 10. Initial redox cycling behavior of BBL-based vOECT. a, Transient curves of the device at a switching frequency of 3.3 Hz. **b**, Swelling behavior of the device at the channel center.

As shown in Supplementary Fig. 10, the channel center is laser-focused on for the initial doping behavior characterization. No evidence of ion injection is observed at the channel center during the first five switching cycles, even though drain currents are continuously enhanced after repeated switching cycles. In subsequent switching cycles, the swelling curve shows a gradual increase in baseline followed by plateauing. This phenomenon indicates that, in a vertical architecture, water molecules and ions need to diffuse stepwise from the electrode edge to the channel center. Specifically, the on-current increases markedly with the number of cycles and then gradually stabilizes during the initial switching cycles.

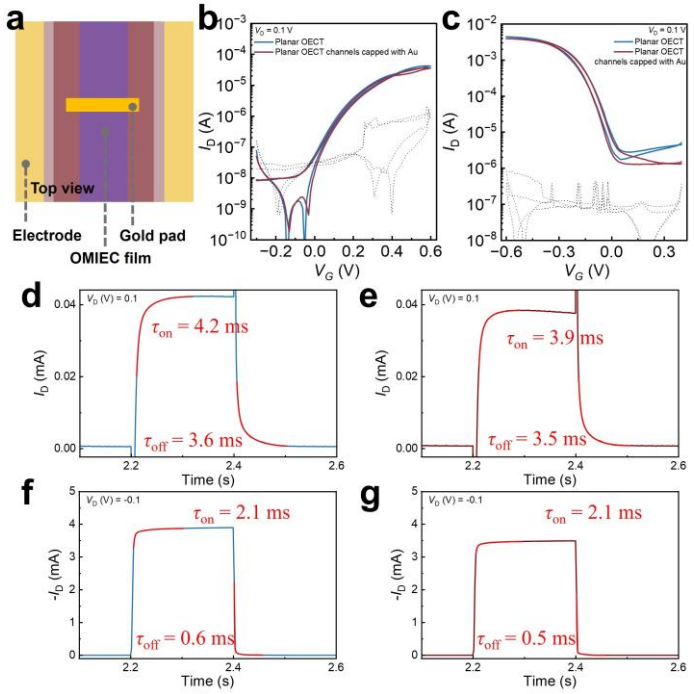

Supplementary Fig. 11. Structural and performance comparison of planar OECTs with and without a reflective gold pad on the channel. a, Schematic of the device structure. Comparisons of transfer characteristics for (**b**) BBL and (**c**) p(g2T-T):DA-based OECTs with and without gold pads. Comparisons of RC time constants for (**d-e**) BBL and (**f-g**) p(g2T-T):DA-based OECTs with and without gold pads. Notably, by depositing a thin gold pad (50 μm length, 20 μm width, and 40 nm thickness) onto the planar OECT channel (channel length × channel width = 20 μm × 500 μm) to serve as a stable optical reflector, the swelling signal can be effectively decoupled from the OMIEC optical property variations.

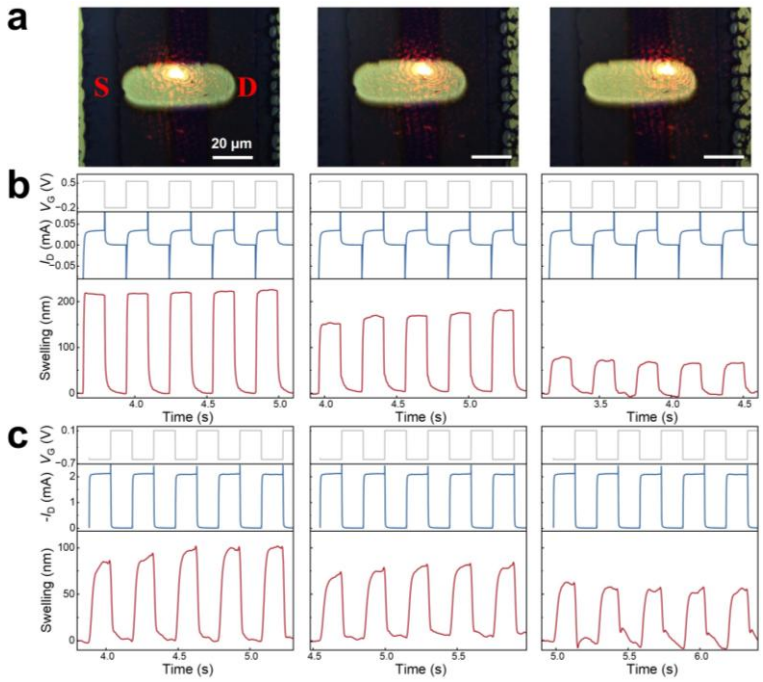

Supplementary Fig. 12. Swell mapping of planar OECT channels. a, Optical images of the laser spot positioned at three locations: near the source side, the channel center, and near the drain side. **b**, Swelling behavior of BBL-based OECTs at the corresponding three positions. **c**, Swelling behavior of p(g2T-T):DA-based OECTs at the corresponding three positions. Notably, the spatial swelling profiles of planar OECTs reveal a distinct gradient (decreasing from source to drain), indicating stronger ionic doping near the source.

Supplementary Table. 2. Summary of active swelling response times of vOECTs with different OMIECs.

Type	Active swelling response time (ms) [a]		
	(3, 3) [b]	(1, 3) [b]	(3, 4) [b]
BBL	22.2±0.4	10.0±0.3	10.3±0.2
Homo-gDPP:GDA	4.8±0.3	4.5±0.5	4.6±0.1
Homo-gDPP:DA	5.0±0.4	4.6±0.3	4.6±0.2
p(g2T-T):GDA	9.1±0.6	2.7±0.3	4.9±0.9
p(g2T-T):DA	21.1±0.8	9.3±0.8	13.4±0.9
gDPP-g2T:GDA	11.1±0.5	7.8±0.4	8.7±0.6
gDPP-g2T:DA	26.3±1.5	18.1±0.5	18.9±0.9

a) Error bars represent standard deviation for n = 5, mean ± s.d.
b) Laser spot position.

The calculation method for the active swelling response time is as follows: First, the moment a doping V_G is applied is taken as the starting time point for active swelling. Then, the moment when active swelling reaches 90% of saturation is chosen as the endpoint. The time difference between these two points is assigned as the active swelling response time.

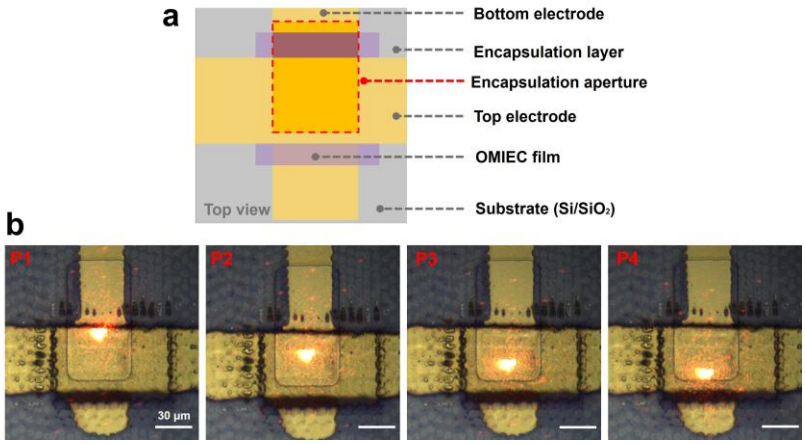

Supplementary Fig. 13. Device structure and laser spot positioning within the channel. a, Schematic of the encapsulation structure where only the upper edge of the top electrode is exposed to the electrolyte solution. **b**, Optical images showing the laser spot sequentially positioned from the electrode edge to the lower edge of the encapsulation aperture (the laser spot is spaced 10 μm apart in each image).

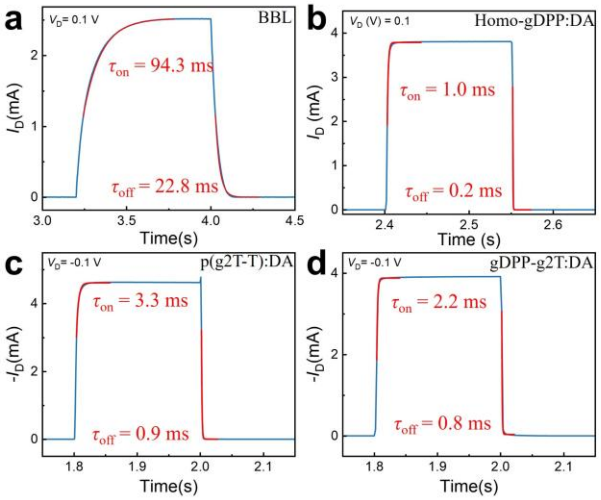

Supplementary Fig. 14. RC time constants of different OMIEC material-based vOECTs. Representative transient curves for vOECTs based on BBL (**a**), Homo-gDPP:DA (**b**), p(g2T-T):DA (**c**) and gDPP-g2T:DA (**d**). Note that these results are based on vOECTs with one side of the top electrode encapsulated, as demonstrated in Supplementary Fig 13.

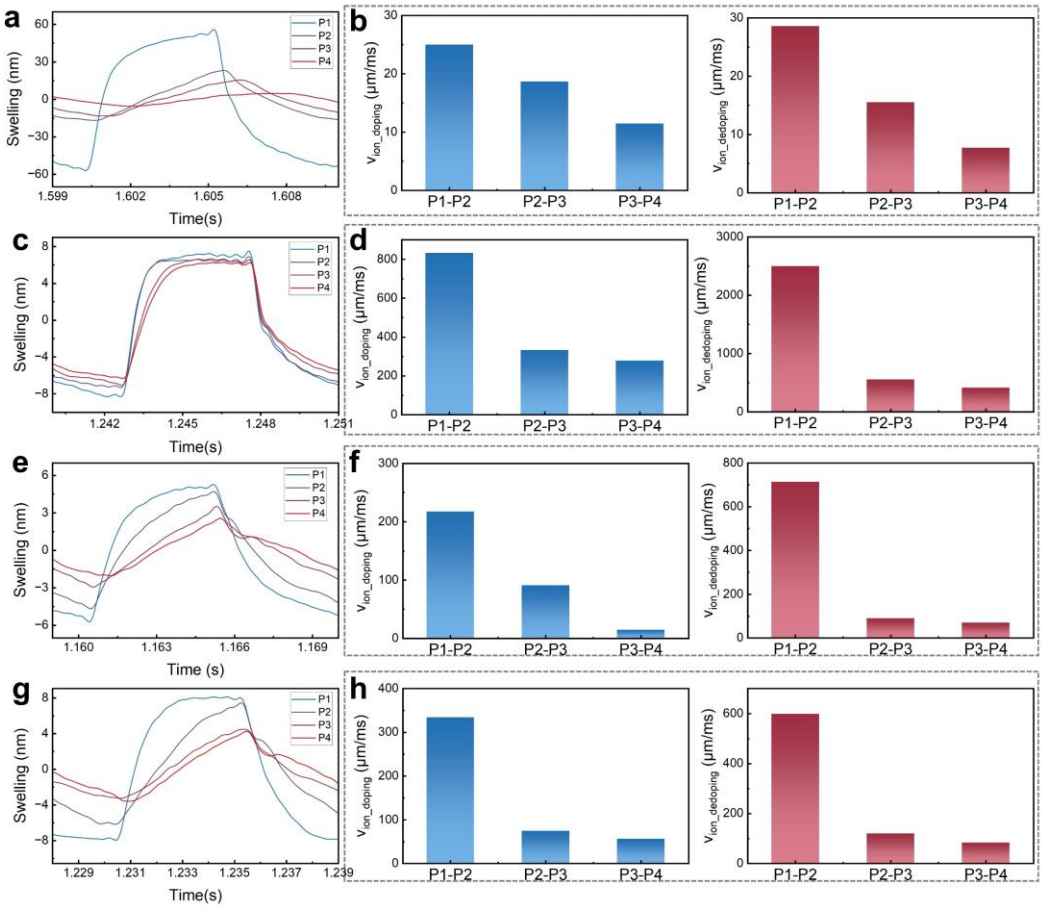

Supplementary Fig. 15. Ion transport in different OMIEC material-based vOECTs. Representative swelling behavior of vOECTs based on BBL (**a**), Homo-gDPP:DA (**c**), p(g2T-T):DA (**e**), and gDPP-g2T:DA (**g**) at four channel positions (P1 to P4, Supplementary Fig 13), which are sequentially spaced 10 μm apart. Rate distribution of ion doping and dedoping (swell moving front) at the above four channel positions for vOECTs based on BBL (**b**), Homo-gDPP:DA (**d**), p(g2T-T):DA (**f**), and gDPP-g2T:DA (**h**). Specifically, the vOECTs based on these four materials are all operated at a switching frequency of 100 Hz. Meanwhile, an LDV-M was used to collect a set of swelling behavior measurements at every 10 μm interval along the channel. For the subsequent calculation of ion transport velocity, the time intervals between the lowest points of each curve were used to determine the ion doping velocity; likewise, the time intervals between the highest points of each curve were adopted to calculate the ion dedoping velocity.

As shown in Supplementary Figs. 14 and 15, we quantified the ion transmission velocity for different OMIECs (BBL, Homo-gDPP:DA, p(g2T-T):DA, and gDPP-g2T:DA) and found a strong positive correlation between this velocity and the device's RC time constant. Specifically, Homo-gDPP:DA exhibits the fastest RC time constants (τ_{on}= 1.0 ms, τ_{off}= 0.2 ms) along with the highest ion transport rate (833.3 μm/ms). In contrast, BBL shows the slowest RC time constants (τ_{on} = 94.3 ms, τ_{off} = 22.8 ms) and the lowest ion transport rate (25.0 μm/ms).

Interestingly, the ion transport velocity across various OMIECs consistently exhibits a decreasing trend from the top channel edge (P1) to the bottom edge (P4) (Supplementary Fig. 13b and 15). Moreover, the ion dedoping velocity is observed to be faster than the ion dedoping velocity, which is consistent with the "slow on, fast off" behavior. Finally, regarding swelling magnitude, distinct differences in swelling characteristics are evident from the top (P1) and bottom (P4) channel edges, a phenomenon particularly pronounced in slow-switching devices such as BBL (Supplementary Fig. 15a). Specifically, as the ion injection distance increases, the swelling behavior gradually transitions from distinct and fast saturation to completely unsaturated.

Note, here we assume the swelling front represents the doping front. Fundamentally, this serves as a physical deformation resulting from the synergistic coupling of ions and water. While not equivalent to a direct and absolute measurement of ion doping level, it effectively reveals the complex doping dynamics trends within OECTs.

Supplementary Table. 3. Summary of active swelling percentage of BBL-based vOECT.

Switching frequency	Swelling percentage at different channel positions	
	(1, y) and (6, y) [a)]	Other positions
3.3 Hz	147.4±20.9%	100.1±18%
11.1 Hz	146.7±19.4%	95±16.9%
111.1 Hz	86±24.9%	26.8±16%

a) y= 1: 4

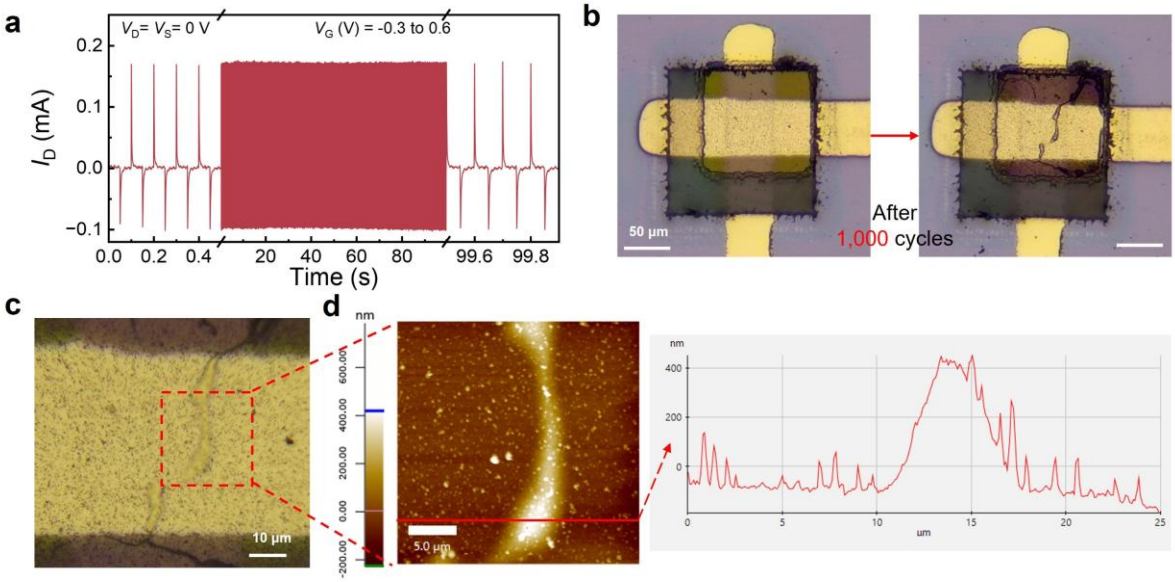

Supplementary Fig. 16. BBL channel morphological variations characterized by optical microscope and AFM. a, I_D transient curve of the device switched 1000 times with $V_D = V_S = 0$V. **b,** Optical images of the device channel area before and after 1000 switching cycles. **c,** Zoomed in optical image of the device channel region after operation, and **(d)** height image characterized by AFM with obvious swelling.

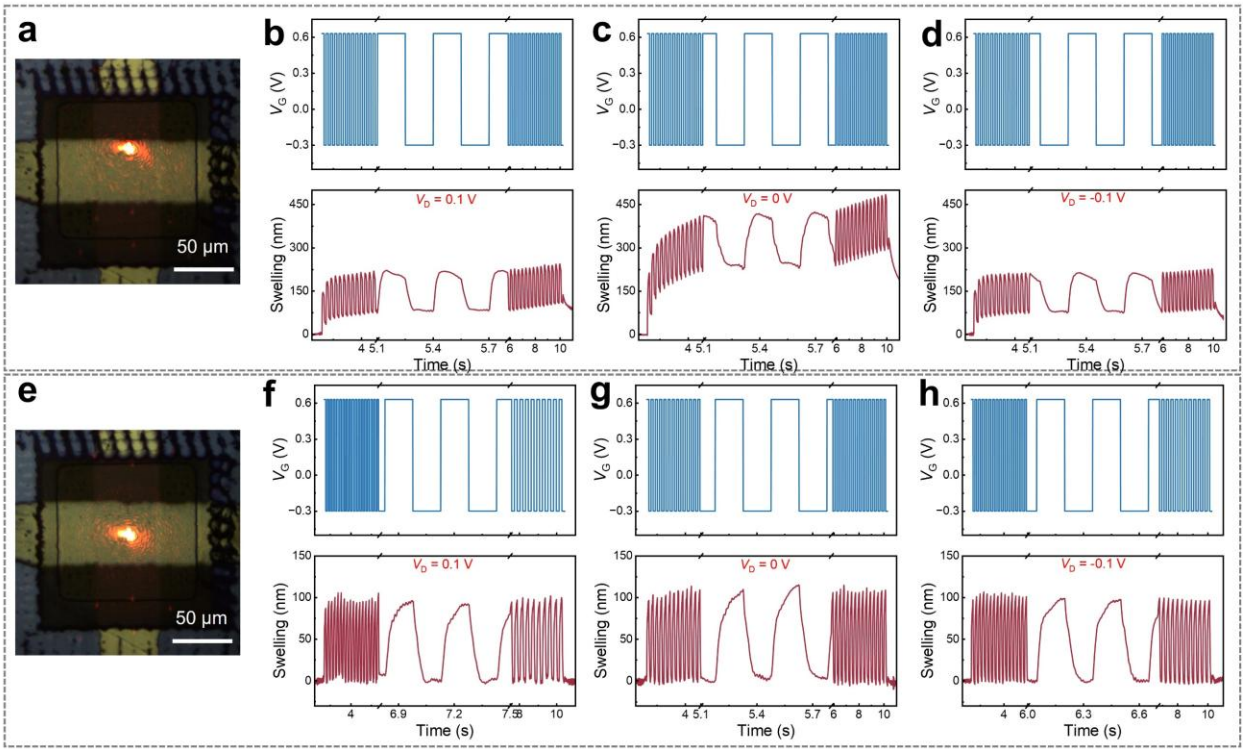

Supplementary Fig. 17. Swelling characteristics of BBL-based vOECT under different drain biases. Optical micrographs of a vOECT depicting the laser spot focused at the channel edge (**a**) and center (**e**). Swelling behavior of BBL-based vOECT at V_D = 0.1 V (**b, f**), 0 V(**c, g**), and -0.1 V(**d, h**).

As shown in Supplementary Fig. 17a-d, at the channel edge, a tremendously large swelling magnitude (as high as 480 nm) is observed under V_D = 0 V, along with a pronounced baseline drift (> 150 nm). Meanwhile, with either V_D = 0.1 V or V_D = -0.1 V, the swelling magnitude is clearly suppressed (< 240 nm).

This observation clearly suggests that the applied drain bias plays a critical role in suppressing film swelling. Furthermore, by comparing the biased conditions (V_D = ±0.1 V), where the absolute magnitude of the applied bias remains constant while the gate-to-drain potential difference varies, we observe that a reduction in the local potential difference would lead to about 4.7% decrease in

swelling magnitude when switching V_D from -0.1 V to 0.1 V. We then characterize the swelling behavior at the channel center (Supplementary Fig. 17e-h). Consistent with the channel edge observations, the highest swelling magnitude (~ 109 nm) is also observed with V_D = 0 V, while ~ 94 nm and ~ 99 nm swelling magnitudes are observed with V_D = 0.1 V and -0.1 V, respectively.

In conclusion, within the unique vertically stacked architecture of vOECT, both the drain-bias-modulated internal distribution and the local gate-to-drain potential difference concurrently influence ion uptake. We hypothesize that the establishment of a vertical Coulombic force may act as a potential mechanism for this suppression, while fully elucidating the exact physical origin warrants further experimental validation.

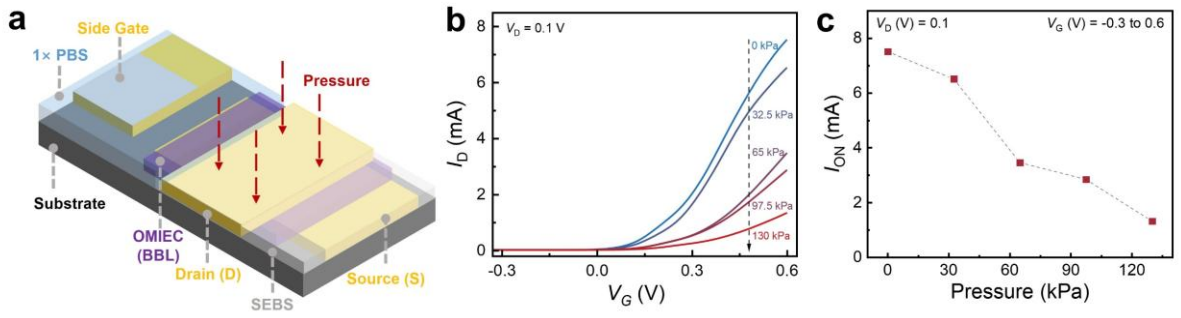

Supplementary Fig. 18. Effect of pressure constraints on operando vOECT performance. (a) 3D schematics of the BBL-based vOECT, illustrating the application of external physical pressure directly onto the top drain electrode during operation. **(b)** Transfer characteristics of the device under varying applied pressures from 0 to 130 kPa, along with **(c)** the corresponding on-state current under different pressures.

An operating OECT channel is highly plasticized by the aqueous electrolyte, drastically altering its mechanical and electrochemical response. Here, we designed a controlled operando experiment (Supplementary Fig. 18a) in which the BBL-based vOECT top electrode surface is encapsulated

with a thin SEBS film. This encapsulation not only allows the electrolyte to be injected from the side opening but also provides essential mechanical protection, preventing the top electrode from tearing or breaking under applied physical pressure. We then applied pressure ranging from 0 to 0.13 MPa on the top electrode of the working vOECT by adjusting the loaded weights (see Methods for details). As shown in Supplementary Fig. 18b,c, the on-state current (I_{ON}) of the vOECT decreases significantly with increasing applied pressure. When the pressure reaches 130 kPa, I_{ON} decreases by a factor of 5.8 (from 7.5 mA to 1.3 mA). This operando measurement clearly demonstrates that for a solvated OMIEC, a pressure as low as 32.5 kPa can suppress swelling and alter device performance.

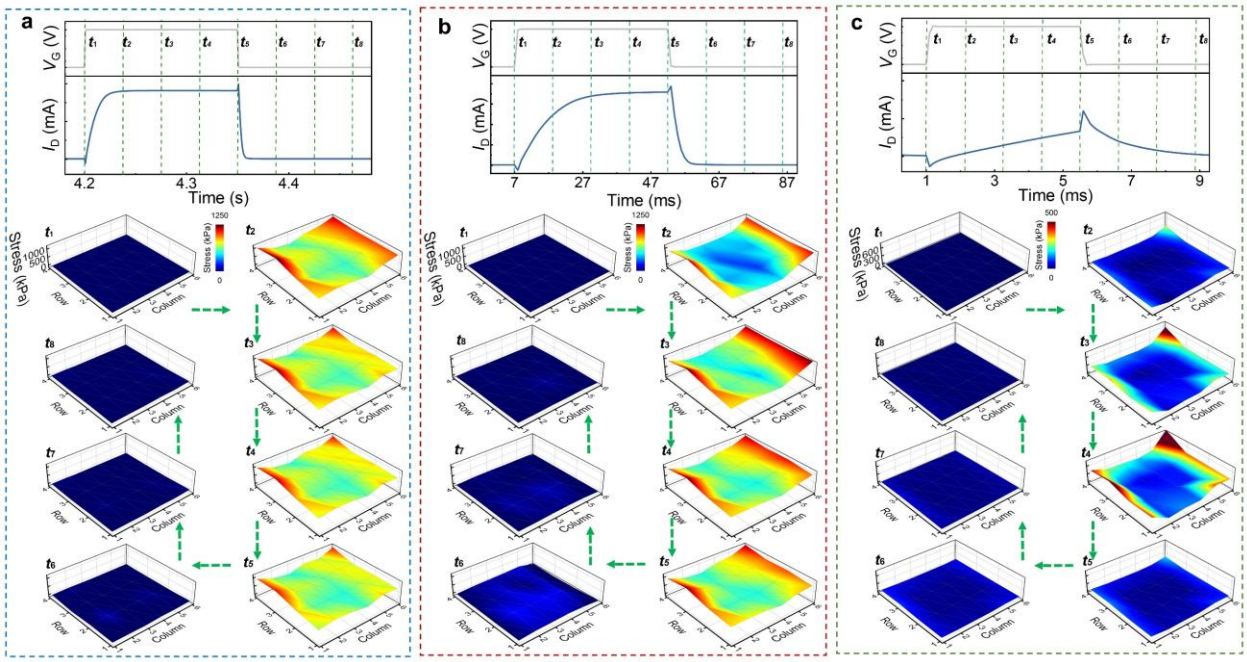

Supplementary Fig. 19. Stress mapping of BBL-based vOECT channel. 3D Stress mapping under **(a)** 3.3 Hz, **(b)** 11.1Hz, and **(c)** 111.1 Hz switching frequencies, along with an I_D switching cycle.

To extract the mechanical stress related to the deformation. First, the Young's modulus of the BBL film in its doped state was characterized using AFM (see Methods for details). Then, recognizing that the E inherently fluctuates during the dynamic (de)doping cycle, we utilized the E value measured in the doped state as a representative baseline to establish the scale of the generated stress. It should be noted that since the dynamic swelling amplitude (ΔL) recorded by our LDV-M platform is exclusively in the vertical direction, the stress (σ) derived here specifically represents the vertical mechanical stress. Crucially, given the inherent sandwiched architecture of the vOECT, the BBL channel is mechanically confined by the top Au electrode. Thus, this calculated σ represents the effective stress generated by the film to overcome the mechanical constraint imposed by the top electrode. According to Hooke's Law, this effective stress can be quantitatively expressed as:

$$\sigma = E\frac{\Delta L}{L}$$

The E was determined to be E = 0.82 MPa, and the passive swelling thickness of the film in solution was measured as L = 145 nm (see Methods for details). By substituting these precise empirical values into the equation, the real-time vertical effective stress is calculated as:

$$\sigma_{BBL} = 0.82\ MPa \times \frac{\Delta L}{145\ nm}$$

Ultimately, combining this with the ΔL continuously recorded by our LDV-M platform, we can now calculate and map the stress. As shown in Supplementary Fig. 19, we present the stress for BBL-based vOECT while operating at 3.3 Hz, 11.1 Hz, and 111.1 Hz switching frequencies.

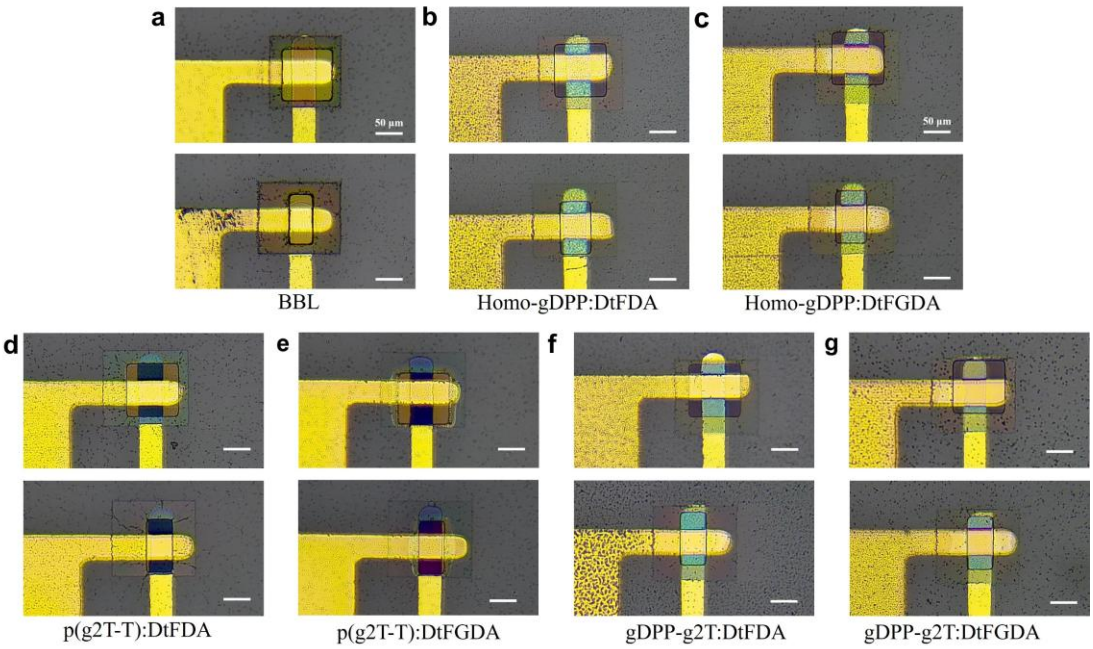

Supplementary Fig. 20. Optical images of vOECTs with conventional and optimized encapsulations. vOECT channels based on **(a)** BBL, **(b)** Homo-gDPP:DA, **(c)** Homo-gDPP:GDA, **(d)** p(g2T-T):DA, **(e)** p(g2T-T):GDA, **(f)** gDPP-g2T:DA, and **(g)** gDPP-g2T:GDA.

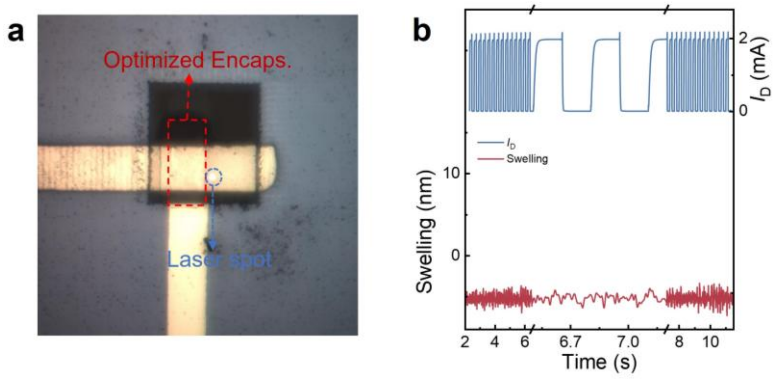

Supplementary Fig. 21. Channel with optimized encapsulation. a, Optical image of the channel, where the red box indicates the encapsulated layer opening and the blue circle marks the position of the laser spot. Notably, the spot is outside the opening of the encapsulated layer. **b,** Swelling behavior of the device at the laser spot position, showing no swelling at this location, indicating that encapsulation can effectively suppress swelling.

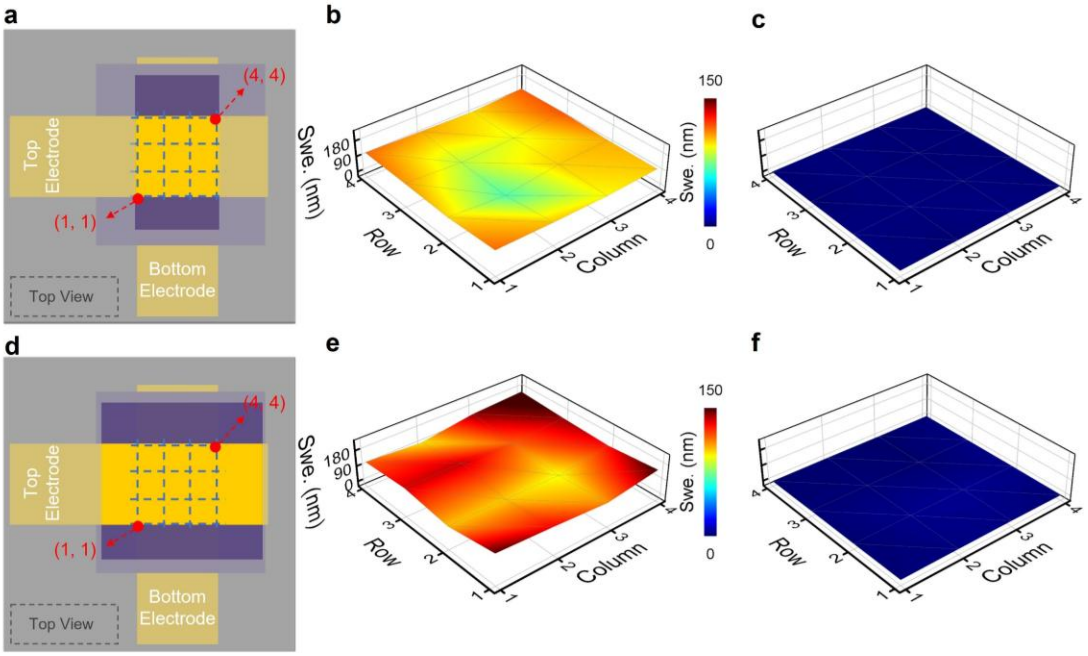

Supplementary Fig. 22. 3D swell mapping of BBL-based vOECTs with different encapsulations. a, Top view of the channel with optimized encapsulation and 4 × 4 mapping point diagram, along with the swell mapping of the channel under **(b)** doping and **(c)** dedoping states under a switching frequency of 3.3 Hz. **d,** Top view of the channel with conventional encapsulation and 4 × 4 mapping point diagram, along with the swell mapping of the channel under **(e)** doping and **(f)** dedoping states with a switching frequency of 3.3 Hz.

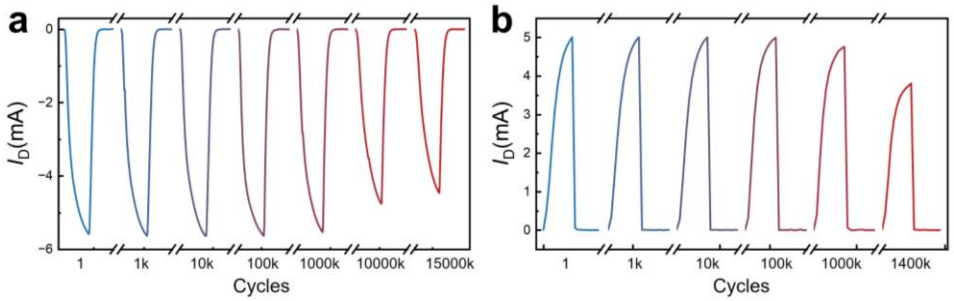

Supplementary Fig. 23. Transient curves for the cycling stability of vOECTs. Representative I_D transient curves of p(g2T-T):DA-based vOECT during 15 M cycling stability tests (**a**) and Homo-gDPP:DA-based vOECT during 1.4 M cycling stability tests (**b**).

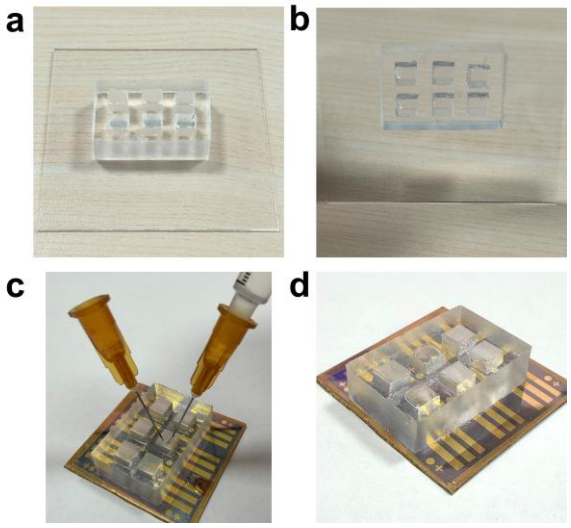

Supplementary Fig. 24. Transient curves for the cycling stability of vOECTs. a–b, Optical images of the PDMS well. **c**, Optical image of electrolyte injection. The electrolyte solution was injected through a right-side syringe, with a left-side needle venting internal air from the well. **d**, Optical image of the PDMS well placed above the vOECT channels.

Supplementary Table 4. Summary of reported cycling stability of OECTs.

Architecture	Transistor type	Material	Cycling number	Operation time (h)	Current retention	Ref
cOECT [a)]	P	h-DPP-g2T	1,500	1.7	/	[5]
	P	PDPP-3EG	600	1.5	99%	[6]
	P	PDPP-4EG	600	1.5	88%	[6]
	P	P3	60	0.2	/	[7]
	P	p(gPyDPP-MeOT2)	400	0.4	92%	[8]
	P	gBDT-MeOT2	300	0.5	93%	[9]
	P	p(g1T2-g5T2)	720	2	98%	[10]
	P	p(g0T2-g6T2)	720	2	98%	[10]
	P	P($g_4$2T-TT)	510	1.4	85%	[11]
	P	p(g3T2):$C_{60}F_{48}$	4,600	25	61%	[12]
vOECT	P	p(g2T-T): DA	100,000	1.1	99%	[13]
	P	gDPP-g2T: Cin-Cell	50,000	1.4	/	[14]
	N	Homo-gDPP: Cin-Cell	50,000	1.4	/	[14]
	P	p(g2T-T): DA	200,000	4.4	/	[15]
	N	BBL/PEI	1M	2.8	97%	[16]
	P	p(g2T-T): DA	1M	13.9	100%	This work
	P	p(g2T-T): DA	5M	69.4	95%	
	P	p(g2T-T): DA	10M	138.9	89%	
	P	p(g2T-T): DA	15M	208.3	82%	
	N	Homo-gDPP: DA	1M	13.9	98%	
			1.4M	19.4	79%	
	N	BBL	126,000	2.8	100%	
			1M	22.2	95%	
			2.8M	62.2	79%	

a) cOECT: conventional planar OECT.

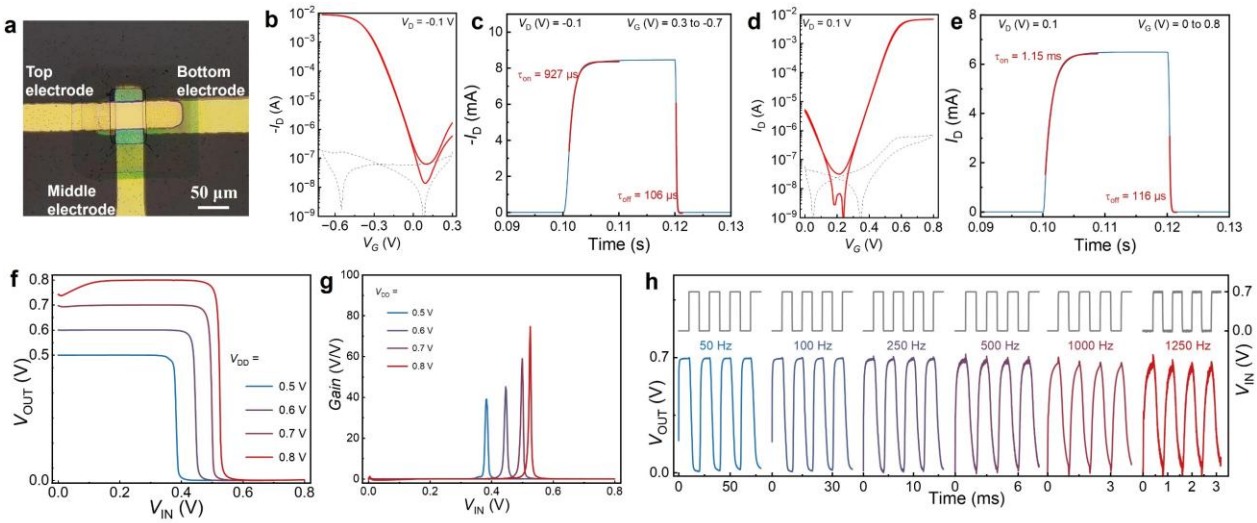

Supplementary Fig. 25. Complementary inverter based on vOECTs with optimized encapsulation. **a,** Microscope image of the inverter. **b,** Transfer and **(c)** transient curves of a p-type vOECT. **d,** Transfer and **(e)** transient curves of an n-type vOECT. **(f)** Voltage transfer curves and **(g)** gain characteristics of the vOECT-based inverter with V_{DD} varying from 0.5 V to 0.8 V. **(h)** Switching behavior of the inverter with V_{IN} switching between 0 V and 0.7 V at frequencies ranging from 50 Hz to 1,250 Hz.

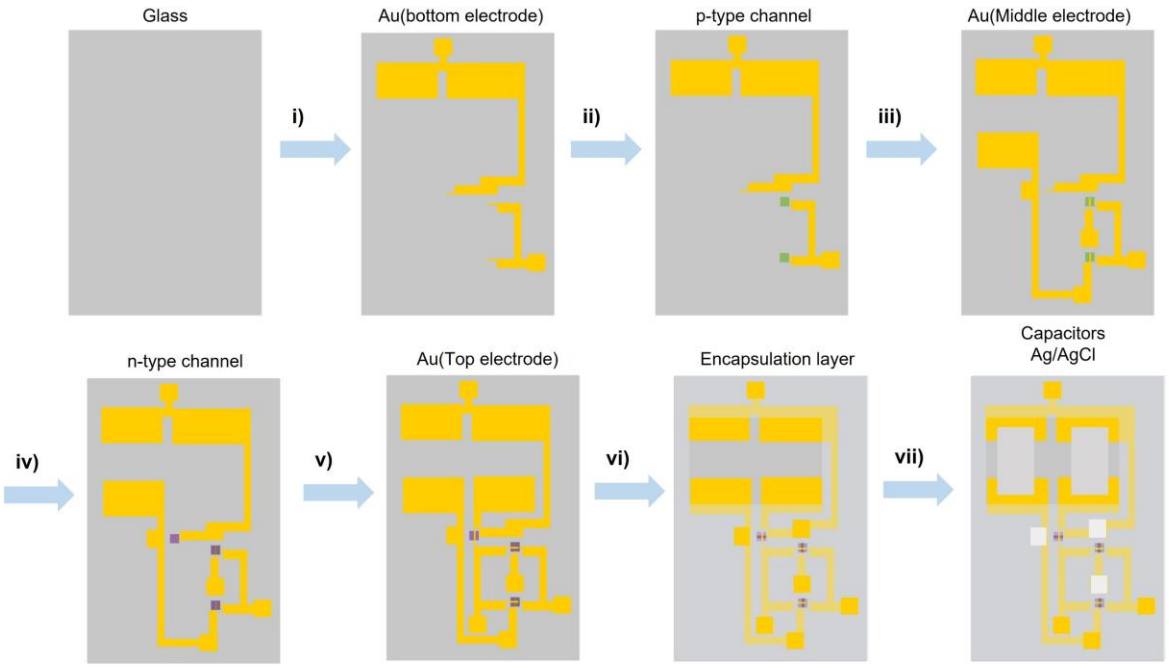

Supplementary Fig. 26. Fabrication process of a vOECN. i) thermal evaporation of the bottom electrodes with a shadow mask; ii) Spin-coating of the p-type semiconducting layer and pattern the polymer with LPKF R4; iii) thermal evaporation of the middle electrodes with a shadow mask; iv) Spin-coating of the n-type semiconducting layer and pattern the polymer with LPKF R4; v) thermal evaporation of top electrodes with a shadow mask; vi) Spin-coating/photopatterning/developing of the SU-8 encapsulation layer, where the channel areas are left open; vii) Drop casting of Ag/AgCl and capacitor pasting.

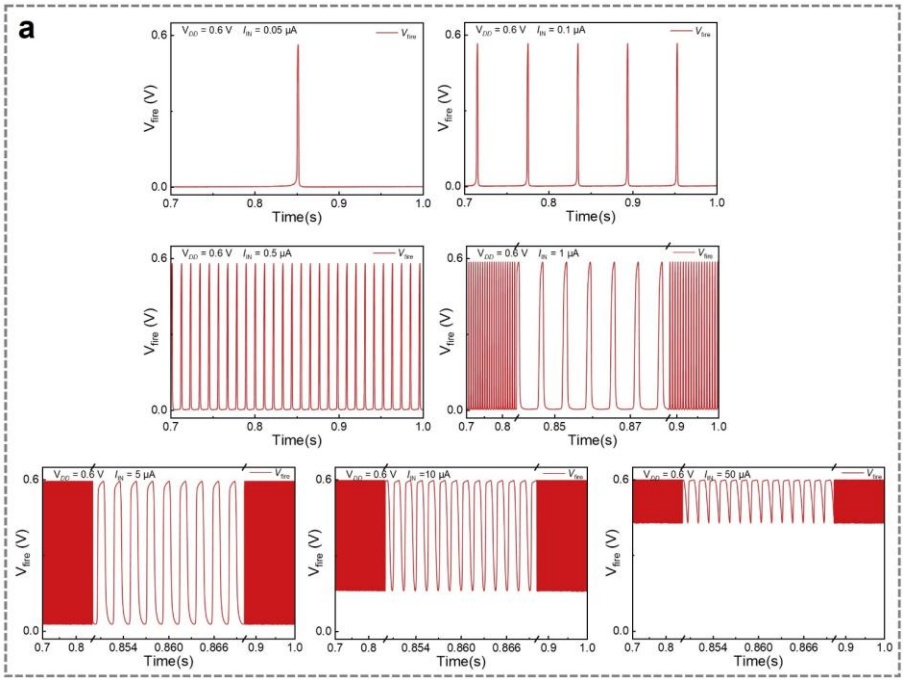

Supplementary Fig. 27. vOECN spiking characteristics. a, Spiking patterns under different input currents at C_{mem} = 500 pF and V_{DD} = 0.6 V.

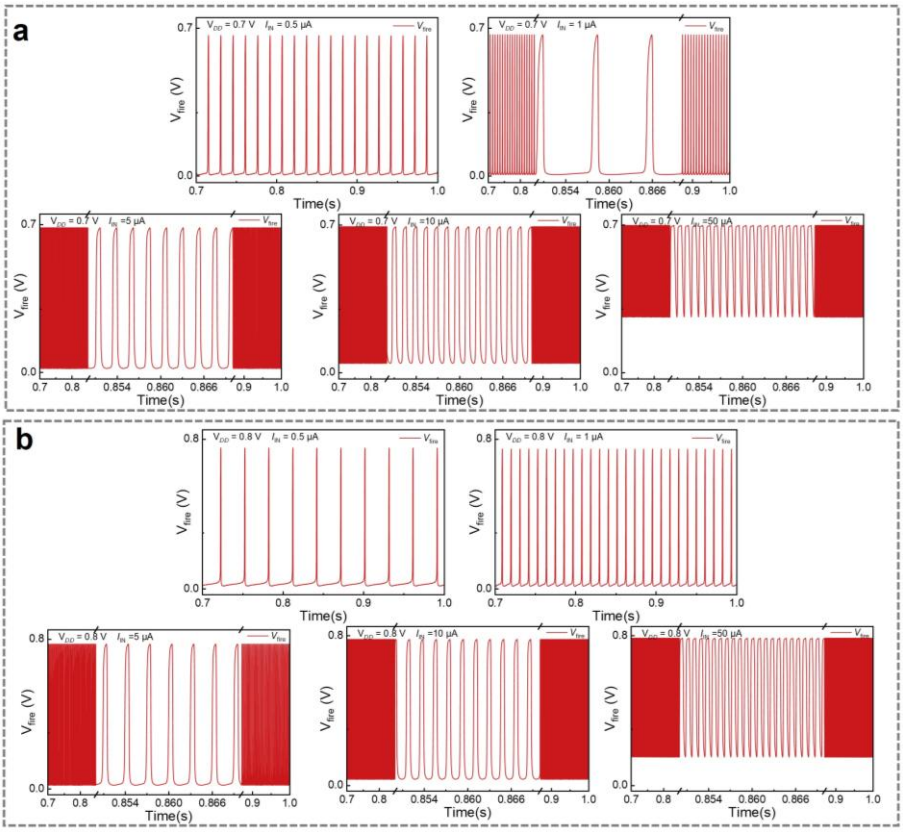

Supplementary Fig. 28. vOECN spiking characteristics. a-b, Spiking patterns under different input currents at C_{mem} = 500 pF and V_{DD} = 0.7, 0.8 V.

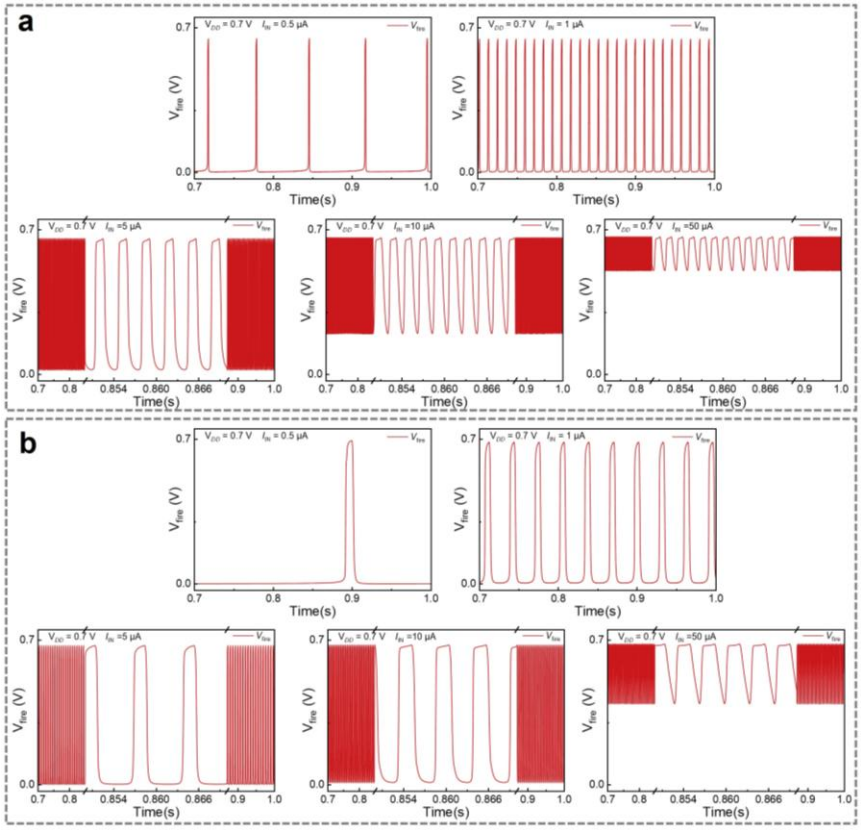

Supplementary Fig. 29. vOECN spiking characteristics. a-b, Spiking patterns at V_{DD} = 0.7 V with I_{IN} = 0.5, 1, 5, 10, 50 μA and C_{mem} = 10, 50 nF.

The vOECN circuit operates as follows: the I_{IN} is integrated through the C_{mem}, thereby gradually increasing the membrane voltage (V_{mem}). When V_{mem} reaches a specific threshold, the output terminal generates neuron-like pulses (V_{fire}). Specifically, the amplification module exhibits a steep increase in gain when V_{mem} exceeds the transition voltage (V_T), driving V_{fire} upward. When V_{fire} reaches a sufficient level, T_{rese} is conducted, discharging C_{mem} and decreasing V_{mem}. Once V_{mem} drops back to V_T, the feedback loop activates, causing V_{fire} to rapidly decrease in response to minor changes in V_{mem}. Eventually, V_{fire} returns to its initial state, T_{reset} turns off, terminating the pulse and initiating the next cycle.

Supplementary Table 5. Types and fire frequency range of different organic neurons.

Type	Membrane capacitance (nF)	Input current (μA)	Fire frequency (Hz)	Footprint (mm^2)	Ref
Multi-order complexity	/	30	32	1.6×10^{-3} (wiring pads excluded)	[17]
	/	1.8	1.4		
Axon- Hillock	1	100	147.1	3.7×10^{1}	[18]
	1,000	0.2	0.13		
	100	10	0.25	1.2×10^{3}	[19]
	10,000	1	0.05		
	0	3	11	/	[20]
	0	0.6	2		
	0	6	1.9	/	[21]
	0	0.25	1		
	0	100	55	/	[16]
	0	5	8		
	2.2	0.3	5.0	5×10^{1}	[22]
	15	0.3	1.0		
	0	0.1	50	1	[23]
	0	32	1,100		
Hodgkin-Huxley	1,000	40	8.3	/	[24]
	2,200	30	1.7		
	1,000	6.3	100	2×10^{2}	[25]
	1,000	2	5		
	100	10	23	/	[26]
	500	3	1.8		
Axon- Hillock	0.5	50	1,111.1	3×10^{1}	This work
	50	0.5	0.5		

References

1 Ngoi, B. K. A., Venkatakrishnan, K. & Tan, B. Laser scanning heterodyne-interferometer for micro-components. *Opt. Commun.* **173**, 291-301 (2000). https://doi.org/https://doi.org/10.1016/S0030-4018(99)00586-6

2 Rothberg, S. J. *et al.* An international review of laser Doppler vibrometry: Making light work of vibration measurement. *Opt. Lasers Eng.* **99**, 11-22 (2017). https://doi.org/10.1016/j.optlaseng.2016.10.023

3 Wu, H.-Y. *et al.* Influence of Molecular Weight on the Organic Electrochemical Transistor Performance of Ladder-Type Conjugated Polymers. *Adv. Mater.* **34**, 2106235 (2022). https://doi.org/https://doi.org/10.1002/adma.202106235

4 Guo, J. *et al.* Understanding asymmetric switching times in accumulation mode organic electrochemical transistors. *Nat. Mater.* **23**, 656-663 (2024). https://doi.org/10.1038/s41563-024-01875-3

5 Chen, J. *et al.* Highly stretchable organic electrochemical transistors with strain-resistant performance. *Nat. Mater.* **21**, 564-571 (2022). https://doi.org/10.1038/s41563-022-01239-9

6 Jo, I.-Y. *et al.* High-Performance Organic Electrochemical Transistors Achieved by Optimizing Structural and Energetic Ordering of Diketopyrrolopyrrole-Based Polymers. *Adv. Mater.* **36**, 2307402 (2024). https://doi.org/https://doi.org/10.1002/adma.202307402

7 He, R. *et al.* Organic Electrochemical Transistor Based on Hydrophobic Polymer Tuned by Ionic Gels. *Angew. Chem. Int. Ed. Engl.* **62**, e202304549 (2023). https://doi.org/https://doi.org/10.1002/anie.202304549

8 Giovannitti, A. *et al.* Energetic Control of Redox-Active Polymers toward Safe Organic Bioelectronic Materials. *Adv. Mater.* **32**, 1908047 (2020). https://doi.org/https://doi.org/10.1002/adma.201908047

9 Giovannitti, A. *et al.* Redox-Stability of Alkoxy-BDT Copolymers and their Use for Organic Bioelectronic Devices. *Adv. Funct. Mater.* **28**, 1706325 (2018). https://doi.org/https://doi.org/10.1002/adfm.201706325

10 Moser, M. *et al.* Side Chain Redistribution as a Strategy to Boost Organic Electrochemical Transistor Performance and Stability. *Adv. Mater.* **32**, 2002748 (2020). https://doi.org/https://doi.org/10.1002/adma.202002748

11 Zhang, S. *et al.* Toward Stable p-Type Thiophene-Based Organic Electrochemical Transistors. *Adv. Funct. Mater.* **33**, 2302249 (2023). https://doi.org/https://doi.org/10.1002/adfm.202302249

12 Le, V. N. *et al.* Improved organic electrochemical transistor stability using solvent degassing and chemical doping. *Nat. Electron.* **8**, 116-126 (2025). https://doi.org/10.1038/s41928-024-01297-8

13 Xie, M. *et al.* Gate bias modulation towards organic electrochemical transistors with ultra-high cycling stability. *J. Mater. Chem. A* **12**, 15753-15761 (2024). https://doi.org/10.1039/d4ta02276a

14 Huang, W. *et al.* Vertical organic electrochemical transistors for complementary circuits. *Nature* **613**, 496-502 (2023). https://doi.org/10.1038/s41586-022-05592-2

15 Gao, L. *et al.* High-loading homogeneous crosslinking enabled ultra-stable vertical organic electrochemical transistors for implantable neural interfaces. *Nano Energy* **129**, 110062 (2024). https://doi.org/https://doi.org/10.1016/j.nanoen.2024.110062

16 Wang, S. *et al.* A high-frequency artificial nerve based on homogeneously integrated organic electrochemical transistors. *Nat. Electron.* **8**, 254-266 (2025). https://doi.org/10.1038/s41928-025-01357-7

17 Ji, J. *et al.* Single-transistor organic electrochemical neurons. *Nat. Commun.* **16**, 4334 (2025). https://doi.org/10.1038/s41467-025-59587-4

18 Yao, Y. *et al.* An organic electrochemical neuron for a neuromorphic perception system. *Proc. Natl. Acad. Sci. U S A.* **122**, e2414879122 (2025). https://doi.org/10.1073/pnas.2414879122

19 Harikesh, P. C. *et al.* Organic electrochemical neurons and synapses with ion mediated spiking. *Nat. Commun.* **13**, 901 (2022). https://doi.org/10.1038/s41467-022-28483-6

20 Liu, T. *et al.* Ground-state electron transfer in all-polymer donor:acceptor blends enables aqueous processing of water-insoluble conjugated polymers. *Nat. Commun.* **14**, 8454 (2023). https://doi.org/10.1038/s41467-023-44153-7

21 Wu, H.-Y. *et al.* Stable organic electrochemical neurons based on p-type and n-type ladder polymers. *Mater. Horiz.* **10**, 4213-4223 (2023). https://doi.org/10.1039/d3mh00858d

22 Mirshojaeian Hosseini, M. J. *et al.* Organic electronics Axon-Hillock neuromorphic circuit: towards biologically compatible, and physically flexible, integrate-and-fire spiking neural networks. *J. Phys. D: Appl. Phys.* **54**, 104004 (2020). https://doi.org/10.1088/1361-6463/abc585

23 Yang, C.-Y. *et al.* High-frequency, low-energy organic event-based sensors for closed-loop neurostimulation. *Nat. Sens.* **1**, 63-72 (2026). https://doi.org/10.1038/s44460-025-00007-x

24 Harikesh, P. C. *et al.* Single organic electrochemical neuron capable of anticoincidence detection. *Sci. Adv.* **11**, eadv3194 (2025). https://doi.org/doi:10.1126/sciadv.adv3194

25 Harikesh, P. C. *et al.* Ion-tunable antiambipolarity in mixed ion-electron conducting polymers enables biorealistic organic electrochemical neurons. *Nat. Mater.* **22**, 242-248 (2023). https://doi.org/10.1038/s41563-022-01450-8

26 Laswick, Z. *et al.* Tunable anti-ambipolar vertical bilayer organic electrochemical transistor enable neuromorphic retinal pathway. *Nat. Commun.* **15**, 6309 (2024). https://doi.org/10.1038/s41467-024-50496-6